

AD-A126 298

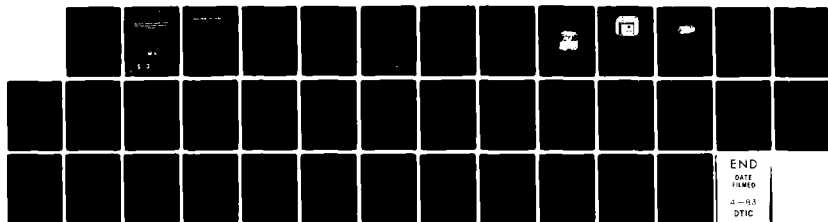
REACTIVELY STEERED ADAPTIVE ARRAY USING MICROSTRIP
PATCH ELEMENTS AT 4 GIGAHERTZ(U) NAVAL WEAPONS CENTER
CHINA LAKE CA R J DINGER FEB 83 NWC-TP-6421

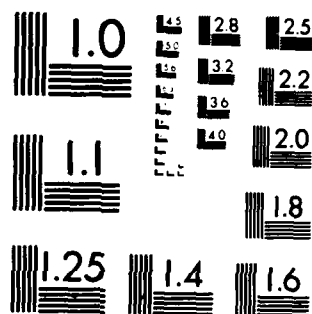
1/1

UNCLASSIFIED

F/G 9/5

NL





MICROCOPY RESOLUTION TEST CHART
NATIONAL BUREAU OF STANDARDS-1963-A

12

NWC TP 6421

Reactively Steered Adaptive Array Using Microstrip Patch Elements at 4 Gigahertz

by
R. J. Dinger
Research Department

FEBRUARY 1983

NAVAL WEAPONS CENTER
CHINA LAKE, CALIFORNIA 93555



Approved for public release; distribution unlimited.

AD A 126298

DTIC FILE COPY

DTIC
ELECTE
APR 4 1983
S B D

88 04 04 038

Naval Weapons Center

AN ACTIVITY OF THE NAVAL MATERIAL COMMAND

FOREWORD

The research described in this report was performed during Fiscal Year 1982 and was supported by Independent Research funding. It is part of a continuing effort to explore novel radio frequency radiating and receiving structures for applications to airborne communication and radar systems.

A. R. Skatvold has reviewed the report for technical accuracy.

Approved by
E. B. ROYCE, *Head*
Research Department
9 February 1983

Under authority of
J. J. LAHR
Capt., U. S. Navy
Commander

Released for publication by
B. W. HAYS
Technical Director

NWC Technical Publication 6421

Published by Technical Information Department
Collation Cover, 18 leaves
First printing 135 unnumbered copies

UNCLASSIFIED

SECURITY CLASSIFICATION OF THIS PAGE (When Data Entered)

REPORT DOCUMENTATION PAGE		READ INSTRUCTIONS BEFORE COMPLETING FORM
1. REPORT NUMBER NWC TP 6421	2. GOVT ACCESSION NO.	3. RECIPIENT'S CATALOG NUMBER
4. TITLE (and Subtitle) REACTIVELY STEERED ADAPTIVE ARRAY USING MICROSTRIP PATCH ELEMENTS AT 4 GIGAHERTZ		5. TYPE OF REPORT & PERIOD COVERED Interim Report on continuing problem
		6. PERFORMING ORG. REPORT NUMBER
7. AUTHOR(s) R. J. Dinger		8. CONTRACT OR GRANT NUMBER(s)
9. PERFORMING ORGANIZATION NAME AND ADDRESS Naval Weapons Center China Lake, CA 93555		10. PROGRAM ELEMENT, PROJECT, TASK AREA & WORK UNIT NUMBERS 61152N
11. CONTROLLING OFFICE NAME AND ADDRESS		12. REPORT DATE February 1983
		13. NUMBER OF PAGES 34
14. MONITORING AGENCY NAME & ADDRESS (if different from Controlling Office)		15. SECURITY CLASS. (of this report) UNCLASSIFIED
		15a. DECLASSIFICATION/DOWNGRADING SCHEDULE
16. DISTRIBUTION STATEMENT (of this Report) Approved for public release; distribution unlimited.		
17. DISTRIBUTION STATEMENT (of the abstract entered in Block 20, if different from Report)		
18. SUPPLEMENTARY NOTES		
19. KEY WORDS (Continue on reverse side if necessary and identify by block number) Adaptive Arrays Anti-jam Techniques Microstrip Antennas Optimization Techniques Parasitic Antennas		
20. ABSTRACT (Continue on reverse side if necessary and identify by block number) See back of form.		

DD FORM 1 JAN 73 1473

EDITION OF 1 NOV 65 IS OBSOLETE
S/N 0102-LF-014-6601

UNCLASSIFIED


SECURITY CLASSIFICATION OF THIS PAGE (When Data Entered)

UNCLASSIFIED

SECURITY CLASSIFICATION OF THIS PAGE (When Data Entered)

(U) *Reactively Steered Adaptive Array Using Microstrip Patch Elements at 4 Gigahertz* (U), by R. J. Dinger. China Lake, Calif., Naval Weapons Center, February 1983. 34 pp. (NWC TP 6421, publication UNCLASSIFIED.)

(U) A reactively steered adaptive array (RESAA) has one element connected by a transmission line to a receiver and a number of closely spaced parasitic elements, each of which is terminated by an adjustable reactive load. The pattern is formed by adaptive control of the reactive loads. A five-element linear RESAA fabricated from microstrip patch antennas was evaluated at 4.0 GHz. Manual adaptive control was used to form a pattern with a minimum in the direction of an interference signal. A minimum could always be formed in the direction of the interference that had a depth (relative to the pattern maximum) of 30 dB and a width of 25 degrees. The theory of the array was developed using an N-port network formalism, and simulations with this theory reproduced the essential features of the experimental measurements. The potential advantages of a RESAA, as compared with a conventional adaptive array, include the elimination of the mixers and other hardware needed to perform the complex weighting of the output of each element at an intermediate frequency, greater dynamic range, and smaller overall size.



UNCLASSIFIED

SECURITY CLASSIFICATION OF THIS PAGE (When Data Entered)

CONTENTS

I. Introduction	3
II. Experimental Microstrip Array Results	4
A. Array Design	4
B. Phase Shifter and Reactive Load Design	4
C. Array Performance	7
III. Reactively Steered Array Theory	13
A. Array Pattern for a General Parasitic Array	13
B. Microstrip Array Pattern	15
IV. Adaptive Control Simulation	18
A. Background	18
B. Error Surfaces	19
C. Steepest Descent Control Algorithm	21
D. Simulation Results	24
V. Conclusions and Future Plans	28
Appendixes:	
A. Measurement of Mutual Impedance Matrix Elements Using an Automatic Network Analyzer	31
B. Radiation Patterns for Two- and Three-Element Reactively Steered Adaptive Arrays	32

Accession For	
NTIS GRA&I	<input checked="checked" type="checkbox"/>
DTIC TAB	<input type="checkbox"/>
Unannounced	<input type="checkbox"/>
Justification	
By	
Distribution/	
Availability Codes	
Dist	Avail and/or Special
A	



I. INTRODUCTION

An essential requirement for many Navy communication and radar receiving systems is the ability to operate in the face of strong intentional interference signals. One technique that has been shown to be capable of providing a margin of 30+ dB against jamming is the use of an adaptive antenna array. Adaptive arrays form their beam in response to the signals impinging on the array; for defeating jammers, the array places pattern nulls in the directions of the undesired jamming signals.

Most adaptive arrays resemble conventional deterministically steered arrays in many respects. Each element has a complex weight, and the weighted element outputs are summed in an electronic summing element to obtain the array output. In the case of an adaptive array, however, the output is processed to derive control voltages that are fed back to the complex weights.

In this report we describe a new type of very compact adaptive antenna array that does not use an electronic summing element. This array, which we term a reactively steered adaptive array (RESAA), differs from other adaptive arrays fundamentally in that only one element is physically connected to a receiver. The remaining elements are parasitic, and the pattern is formed according to the values of the reactive terminations on these parasitic elements. The array "summing" occurs in the currents on the one element connected to the receiver; thus, the electronic summing device is eliminated.

This report discusses experimental results and the supporting theory for a RESAA consisting of five microstrip rectangular patch elements. The array operates at a frequency of 4.0 GHz. This array is intended primarily as a generic form of a RESAA to demonstrate the capabilities of the technique and to use as a test bed for development of an automatic control method. However, because of their low profile, microstrip elements are increasingly being favored for flush-mounted conformal antennas on missiles and aircraft. The application of adaptive array techniques to microstrip elements is of particular interest, because the mitigation of jammers using adaptive beam-forming techniques helps to overcome the vulnerability to jamming that the relatively narrow bandwidth of microstrip elements permits.

This report is organized as follows. The next section describes the experimental results obtained using manual adjustment of the

reactive terminations on a five-element microstrip array. Section III presents the theory describing the operation of a RESAA. This theory is used to interpret the experimental results of the microstrip array, but a detailed comparison of theory and experiment is not attempted. Rather, the theory is used in Section IV to analyze one possible automatic adaptive control method that could be used with any RESAA. In Section V a discussion is given of future plans and recommendations.

II. EXPERIMENTAL MICROSTRIP ARRAY RESULTS

A. ARRAY DESIGN

To demonstrate the RESAA concept, the microstrip array shown in Figure 1 was fabricated and tested using manual control of the phase shifter reactive loads. The elements were designed to have a center frequency at 4.0 GHz, a frequency chosen as a reasonable tradeoff between a convenient antenna size, fabrication ease of phase shifters and antenna elements, and availability of an anechoic chamber for testing. The spacing of 0.75 cm corresponds to a separation of 0.1λ at 4.0 GHz; the experimental coupling results of Jedlicka *et al.*,¹ along with extrapolation of our earlier experience² with arrays at 20 MHz, indicated that this separation would produce a sufficient amount of mutual coupling between elements. The substrate material is Rexolite 1422 with a thickness of 1.58 mm.

B. PHASE SHIFTER AND REACTIVE LOAD DESIGN

A variable reflection phase shifter terminating a transmission line with a characteristic impedance Z_0 produces a variable reactance X according to the equation

$$X = Z_0 \tan \phi \quad , \quad (1)$$

where ϕ is the phase shift. Microstrip phase shifters were designed and fabricated to provide the necessary amount of phase shift, using a

¹ R. P. Jedlicka, M. T. Poe, and K. R. Carver. "Measured Mutual Coupling Between Microstrip Antennas," *IEEE Trans. Antennas Propag.*, Vol. AP-29 (Jan 1981), pp. 147-149.

² Naval Research Laboratory. "A Compact HF Antenna Array Using Reactively Terminated Parasitic Elements for Pattern Control," by R. J. Dinger and W. D. Meyers. Washington, DC, NRL, May 1982. (NRL Memo Report 4797, publication UNCLASSIFIED.)

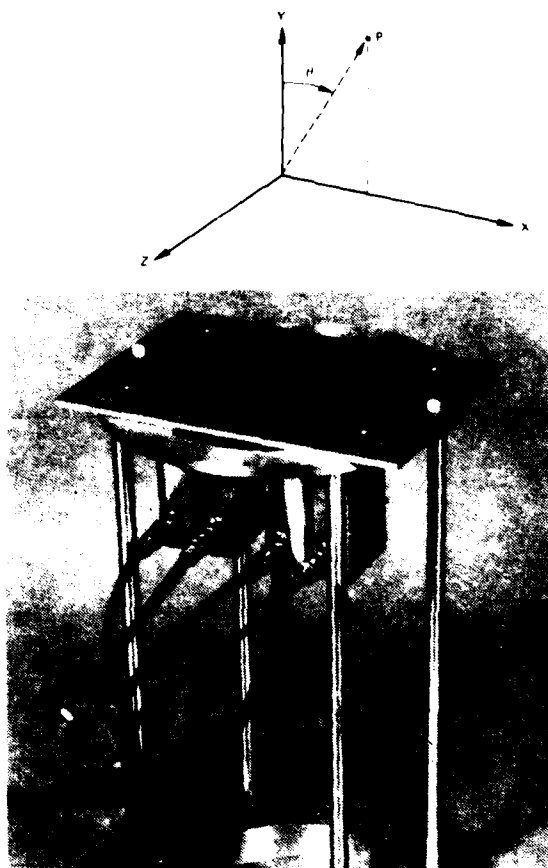


FIGURE 1. Experimental RESAA and
Diagram of Antenna Coordinate System.
P denotes the field observation point.

varactor diode mounted between a 50-ohm microstrip line and the ground plane. Figure 2 is a photograph of the phase shifter, and Figure 3 displays the phase shift versus control voltage characteristic of three of the finished devices. The control characteristic is clearly not linear, but a linear characteristic is not required for this array because it is adaptive (i.e., precise knowledge of the conversion between control voltage and phase shift is not needed in forming the antenna pattern). However, better linearity than is evident in Figure 3 would be desirable for best performance, since most of the phase control

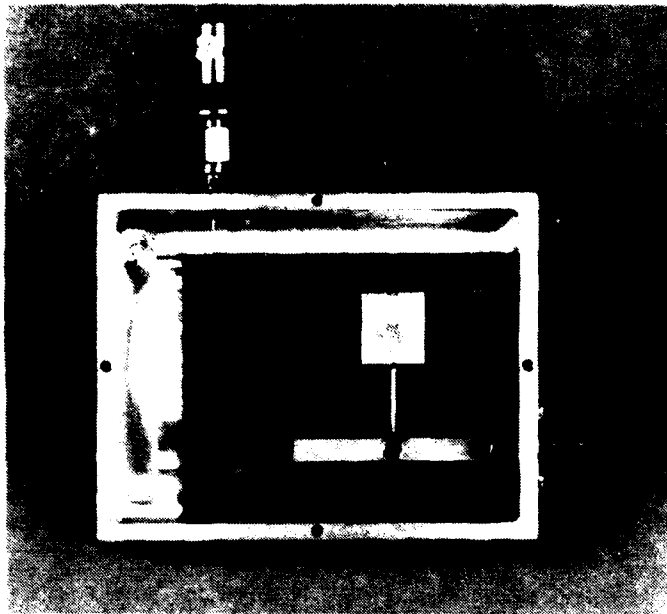


FIGURE 2. Microstrip Phase Shifter.

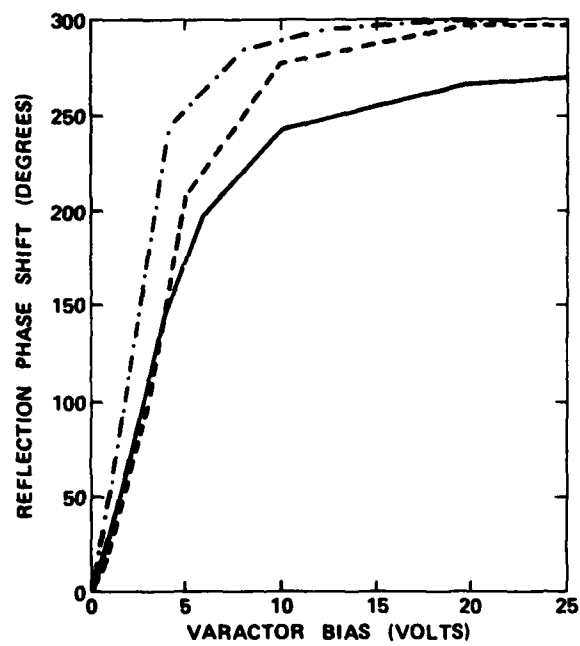


FIGURE 3. Reflection Phase Shift as a Function of Varactor Bias Voltage for Three Units.

occurs only in about 6 volts of the 30-volt bias range. A linear control characteristic requires at least two varactor diodes,³ a complication that was felt unwarranted for this proof-of-concept array. The reflection loss for the phase shifters was typically less than 1.5 dB.

Figure 4 is a photograph of the rear of the array, showing the four phase shifters connected to the feeds of the four parasitic elements.

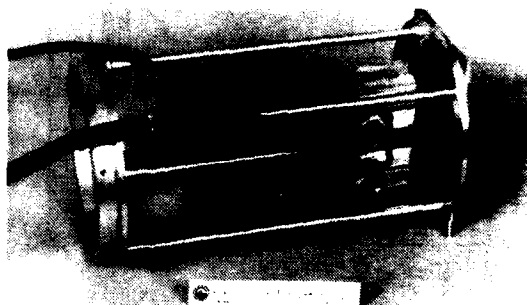


FIGURE 4. Rear View of Experimental RESAA Showing Phase Shifters in Place.

C. ARRAY PERFORMANCE

A block diagram of the installation of the array in an anechoic chamber is shown in Figure 5. All antenna patterns shown in this report were taken in the H-plane of the array. The measurements proceeded in three steps. (1) The array was rotated in the θ -plane to place the incident angle of the anechoic test signal in a direction to represent an interference signal. (2) The array output (as produced by the mixer-receiver combination) was then monitored and the control voltages for the phase shifters iteratively adjusted to minimize its value. Typically, about three passes through the four phase shifter voltage adjustments were enough to decrease the signal level to its lowest value. (3) The phase shifter voltage levels were left untouched (i.e., the reactive terminations were "frozen"), and the anechoic chamber test signal was then used to record the antenna pattern.

³ R. V. Garver. "360 Degree Varactor Linear Phase Modulator," *IEEE Trans. Microwave Theory Tech.*, Vol. MTT-17 (March 1969), pp. 137-147.

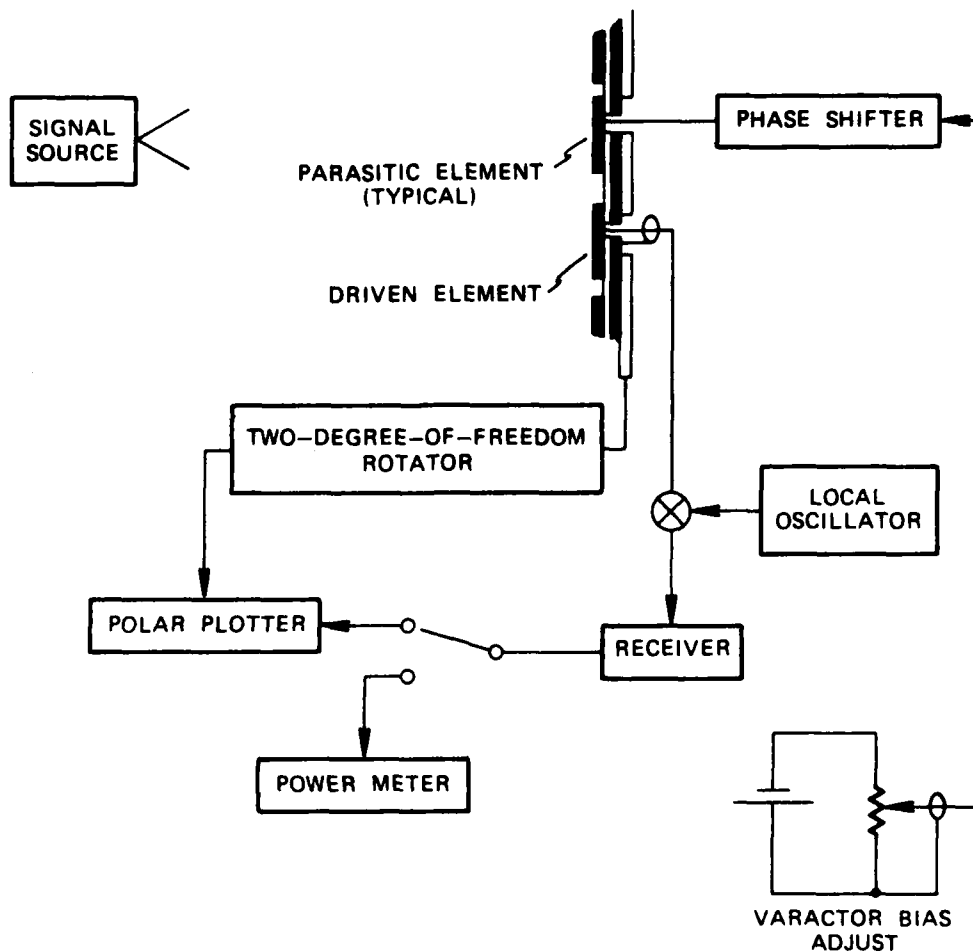


FIGURE 5. Diagram of the Installation of the Experimental RESAA in an Anechoic Chamber.

The results of this process are shown in Figure 6. Recorded patterns are given for incident signal angles of 0, 30, 45, and 60 degrees. The adjustment of the reactive terminations is observed in these patterns to place a minimum in the pattern towards the direction of the interference source. This minimum has a width of about 25 degrees and a depth (as measured relative to the average pattern amplitude) of about 30 dB. The other relatively minor features in the patterns result from unused degrees of freedom; that is, more than one set of reactive termination values will produce the desired minimum in the pattern, and control over features other than the minimum requires additional information to choose the correct set of termination values.

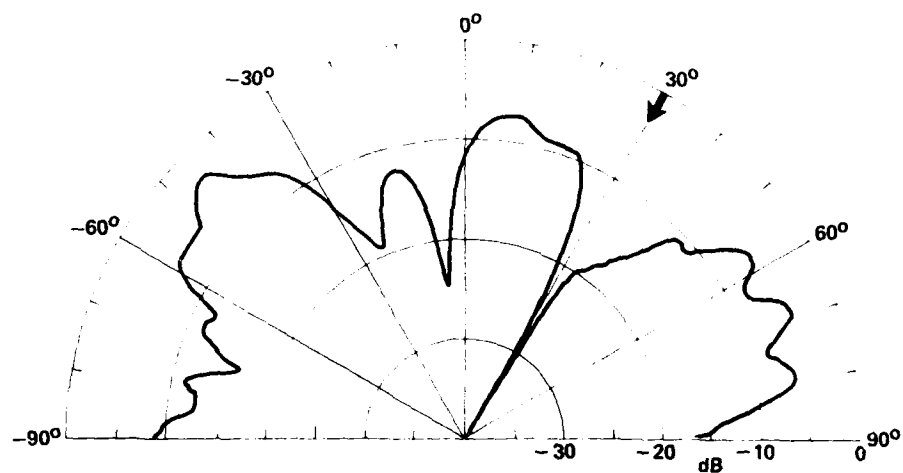
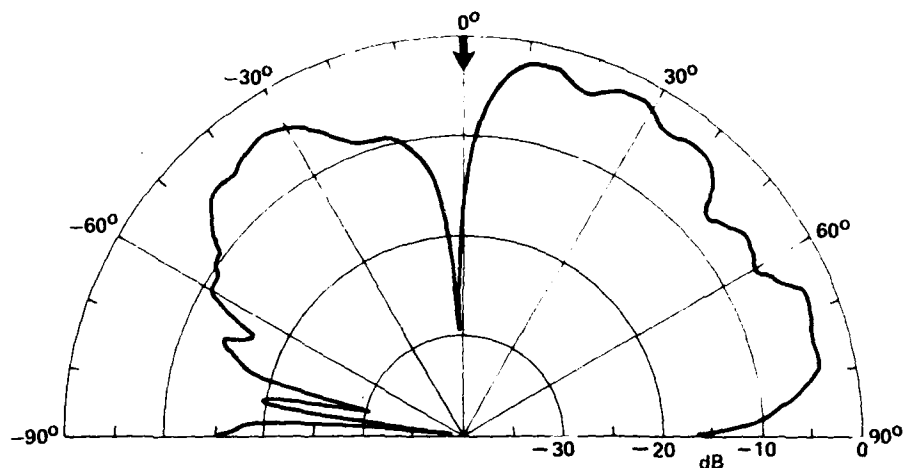


FIGURE 6. Log-Polar Plots of the Measured Radiation Pattern After a Signal Incident in the Direction Indicated by the Arrow was Minimized by Reactive Load Adjustment: 0- and 30-Degree Incidence. 0 dB is an incident power of 7.0 dBi, as measured by a standard gain horn.

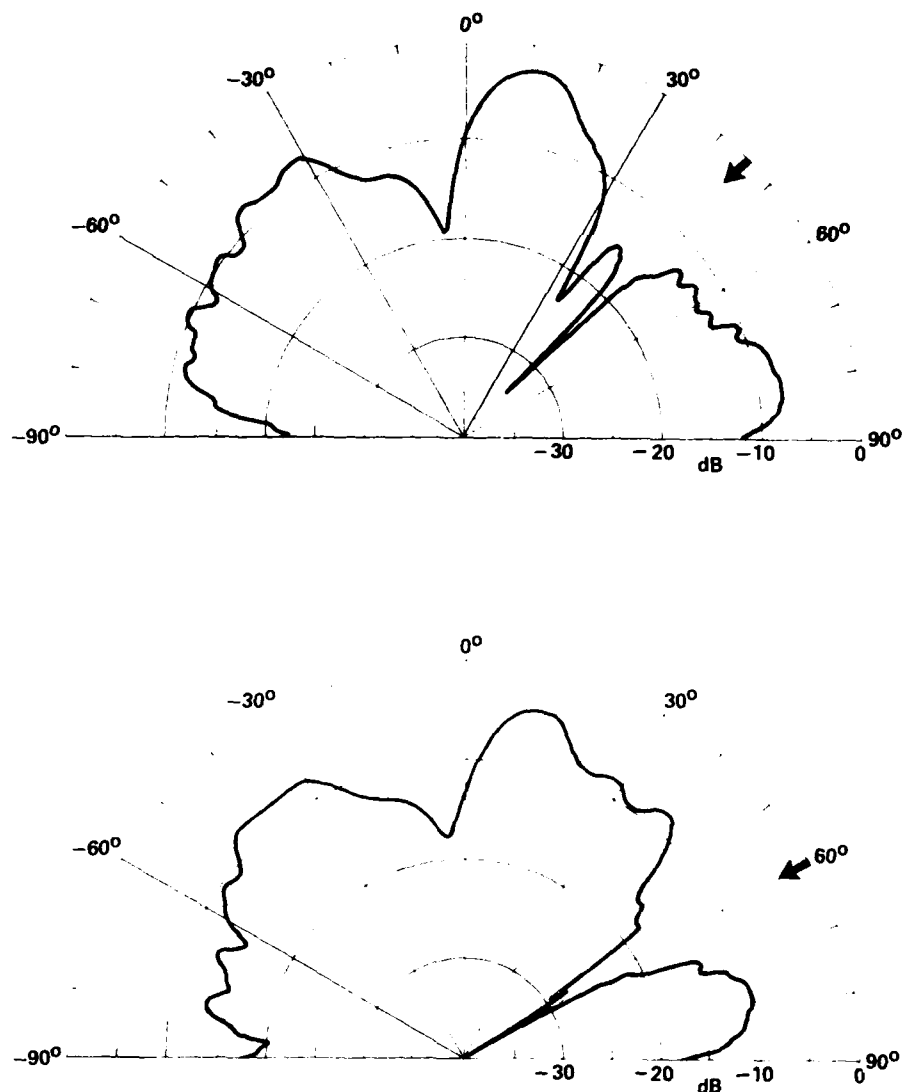


FIGURE 6 (Contd). Log-Polar Plots of the Measured Radiation Pattern After a Signal Incident in the Direction Indicated by the Arrow was Minimized by Reactive Load Adjustment: 45- and 60-Degree Incidence. 0 dB is an incident power of 7.0 dBi, as measured by a standard gain horn.

Figure 7 shows the sensitivity of the pattern minimum to frequency. In this figure, an incident signal at 3.95 GHz was nulled and the reactive terminations frozen. Patterns were then measured at the frequencies on both sides of 3.95 GHz. Figure 7 indicates that as the frequency is changed from that at which the null was formed, the minimum shifts in direction and the depth of the minimum decreases.

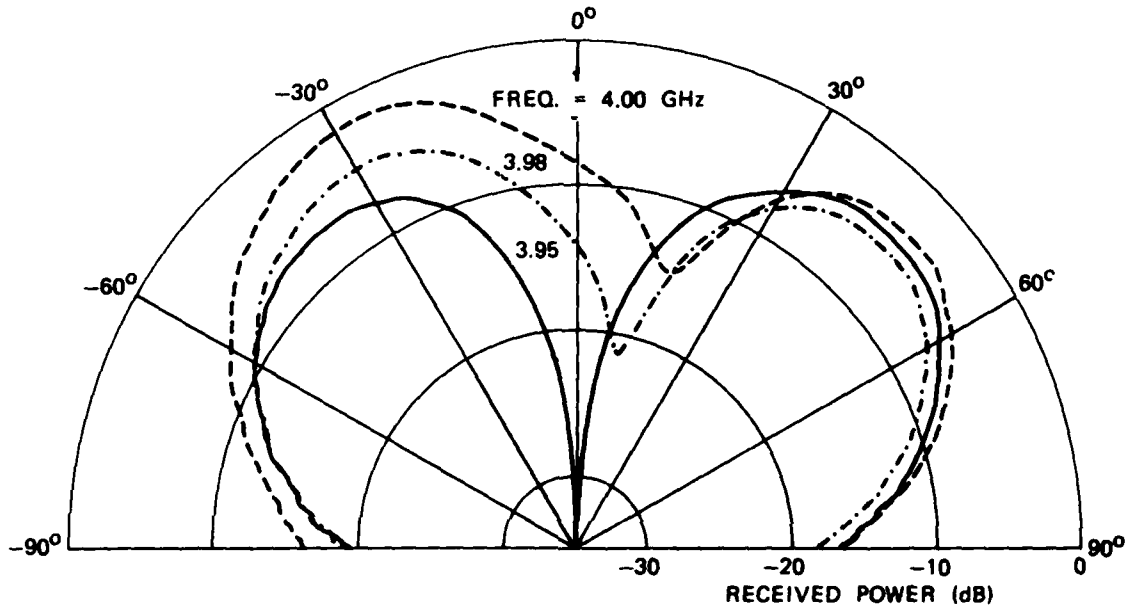


FIGURE 7. Log-Polar Plot of the Measured Radiation Pattern for Three Frequencies. The reactive loads were adjusted at a frequency of 3.95 GHz and left untouched for the other two frequencies.

Figure 8 is a plot of pattern value at the minimum point versus frequency; defining the nulling bandwidth as the frequency range over which the null is at least 20 dB below the pattern maximum, a value of about 40 MHz is obtained for this array.

To summarize the experimental results, the following points are emphasized.

- The interference nulling procedure consistently resulted in an antenna pattern with a null that was narrow (25 degrees) and reasonably deep (at least 30 dB).
- The null could be steered to essentially any angle of incidence, except for grazing incidence on the antenna ground plane.

- No noticeable decrease in array efficiency was detected because of the closely coupled parasitic elements. That is, the parasitic elements and the phase shifter terminations do not introduce additional loss into the array.

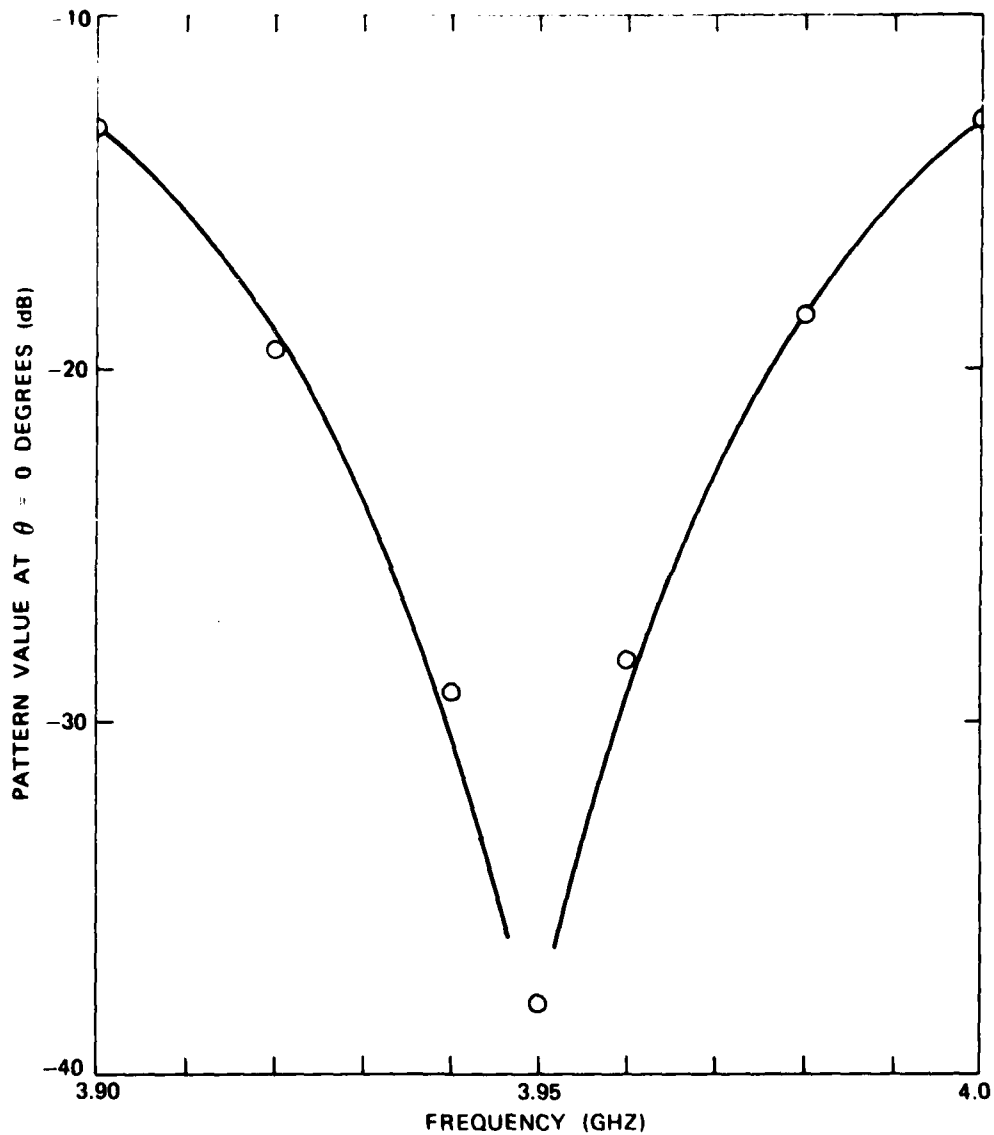


FIGURE 8. Pattern Amplitude at $\theta = 0$ as a Function of Frequency for Signal Minimized at $\theta = 0$ Degrees at a Frequency of 3.95 GHz.

In the next section, equations are derived for the radiation pattern of a RESAA, both for a general form of array element and, specifically, for a microstrip patch element; the pattern is expressed as a function of the reactive termination loads on the parasitic elements. We do not attempt a point-by-point fit between the experimentally measured patterns and the patterns predicted by the theory. We will note that the general behavior predicted by the theory is observed in the experimental measurements and then proceed to use the theory to devise and evaluate an automatic adaptive control technique for the RESAA.

III. REACTIVELY STEERED ARRAY THEORY

Harrington⁴ first presented the theory for an array of reactively steered (wire) dipole antennas and later⁵ extended this theory to an array of dielectrically loaded waveguide-fed slot antennas. All of his analyses treated the array deterministically in the sense that reactive load selection was accomplished by an open-loop technique. In this section, we extend Harrington's analysis to the microstrip array.

A. ARRAY PATTERN FOR A GENERAL PARASITIC ARRAY

In analyzing the wire dipole array,⁴ Harrington used the Thevenin equivalent circuit of Figure 9, which shows a load network and an N-port antenna system connected in parallel with series-driving voltages. The terminal equation for the load and antenna system of Figure 9 is

$$\vec{V}^{oc} = [Z_A + Z_L] \vec{I} \quad , \quad (2)$$

where \vec{V}^{oc} and \vec{I} are the column vectors of the Thevenin equivalent voltages and port currents, respectively. The matrices $[Z_A]$ and $[Z_L]$ are the open-circuit impedance matrices of the antenna system and load system, respectively. The electric field radiated by the antenna system can then be written by superposition as

$$\vec{E} = \sum_{n=1}^N I_n \vec{E}_n^{oc} \quad , \quad (3)$$

⁴ R. F. Harrington. "Reactively Controlled Directive Arrays," *IEEE Trans. Antennas Propag.*, Vol. AP-26 (May 1978), pp. 390-547.

⁵ J. Luzwick and R. F. Harrington. "A Reactively Loaded Aperture Antenna Array," *IEEE Trans. Antennas Propag.*, Vol. AP-26 (July 1978), pp. 870-873.

where \vec{E}_n^{oc} is the field radiated when a unit current exists at port n and all other ports are open circuited. Equation 2 can be inverted and solved for \vec{I} and substituted into Equation 3 to give

$$\vec{E} = \vec{E}^{oc} [Z_A + Z_L]^{-1} \vec{V}^{oc} \quad (4)$$

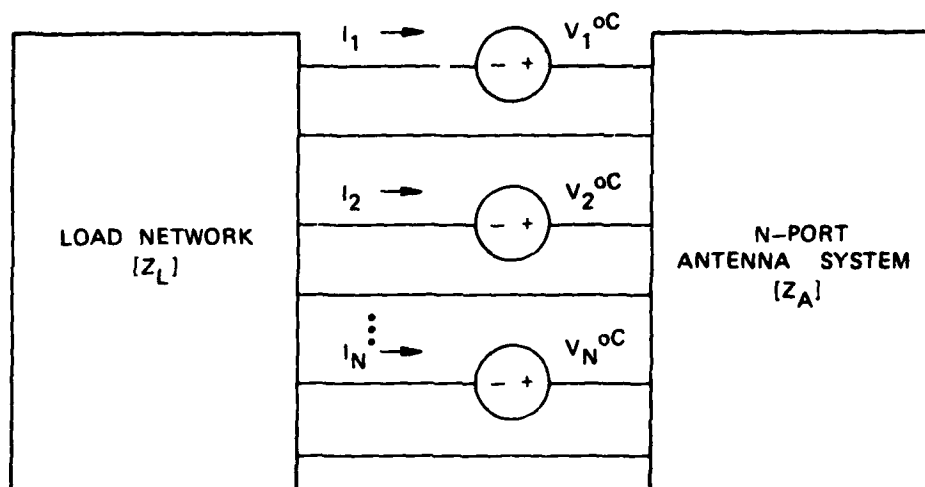


FIGURE 9. Thevenin Equivalent Circuit of an Antenna Array with Parasitic Elements.

Since only the center element denoted by $p = (N + 1)/2$ is driven in this array, \vec{V}^{oc} is a vector with all zeros except for the p^{th} element. Hence, Equation 4 can be written as

$$\vec{E} = V_p \sum_n \vec{E}_n \{ [Z_A + Z_L]^{-1} \}_{np} \quad (5)$$

where $\{-\}_{np}$ denotes the np element of the matrix $[Z_A + Z_L]^{-1}$ and V_p is the open-circuit voltage at the center-driven element. For a given type of antenna element and array geometry, Equation 5 can be used to determine the (unnormalized) array pattern by computing the elements of $[Z_A]$ and $[Z_L]$ and substituting the appropriate form for \vec{E}_n .

B. MICROSTRIP ARRAY PATTERN

This method of analysis using N-port network theory clearly is suitable for wire antennas and lumped element loads; it was used,² for example, to synthesize antenna patterns at 20 MHz. The applicability of the theory to aperture antennas and transmission line loads is not obvious; however, Harrington and Mautz⁶ have shown that N-port network theory can be used for aperture problems by dividing the analysis into two separate regions by using the equivalence principle. One region contains only the loads (i.e., the space "behind" the aperture), and the other region is the half-space into which the array radiates. Two aperture impedance matrices are computed, one for each region, that are independent of each other. Luzwick and Harrington⁵ used this approach to analyze a reactively steered array of dielectrically loaded waveguide-fed slot antennas and arrived, after a lengthy analysis, at an equation of the same form as Equation 5 (actually, the admittance equation that is the dual of Equation 5, since they chose to use an admittance formulation). Therefore, without proceeding through a complete derivation starting from equivalent current sheets for the microstrip patch elements, we assert that Equation 5 can be used directly to write down the array radiation pattern. The task then is to derive expressions for (1) $[Z_A]$, the diagonal matrix of reactive terminations, (2) $[Z_L]$, the mutual impedance matrix for the radiation half-space, and (3) \vec{E}_n , which is equivalent to the radiated electric field of an isolated microstrip patch element.

1. Load Matrix $[Z_L]$

The load matrix has the form $(Z_L)_{ij} = Z_{Li} \delta_{ij}$, except that $Z_{Lp} = 0$, corresponding to the driven element (assumed to be matched). The form of each load is given by Equation 1, so that the entries along the diagonal of $[Z_L]$ can be written compactly as

$$(Z_L)_{ii} = jZ_o \tan \phi_i \quad , \quad (6)$$

where ϕ_i is the phase shift for the i^{th} element.

⁶ R. F. Harrington and J. R. Mautz. "A Generalized Network Formulation for Aperture Problems," *IEEE Trans. Antennas Propag.*, Vol. AP-24 (Nov 1976), pp. 870-873.

2. Mutual Impedance Matrix $[Z_A]$

Several techniques for computing the mutual impedance between microstrip patch antenna elements have been reported,⁷⁻¹⁰ all of which require considerable machine computation and none of which can be written down in convenient analytical form. The equations due to Krowne and Sindoris¹⁰ are the most straightforward; however, their applicability is somewhat limited, since the equations are apparently valid only for very closely spaced elements. For design and analysis of arbitrary patch arrays, theoretical expressions for the mutual impedance over a wide range of array parameters are needed. Although we have done some calculations using the equations in Reference 10, the calculations presented below have avoided the problem by using mutual impedance matrix values obtained by *measurements* on the experimental antenna shown in Figure 1. These measurements were taken using an automatic network analyzer, a discussion of which is given in Appendix A.

3. Radiation Field E_n

We use a transmission line model of a microstrip patch element¹¹ with the coordinate system shown in Figure 1. Radiation occurs mainly from fringing fields at the open-circuited ends, and each end is assumed to radiate as a dipole element. The total radiated field from one patch element is then given by the superposition of two dipole fields separated by the patch width L . To within a factor that is constant for all elements, the radiation pattern for E_z is given by

$$(E_z)_n = \frac{2\sin(k_o h \cos\theta/2)}{k_o h \cos\theta} \cos(k_o L \cos\theta/2) e^{jk_o x_n \cos\theta}, \quad (7)$$

where h is the substrate thickness and $k_o = 2\pi/\lambda$. The exponential factor in Equation 7 accounts for the phase variation across the array, with the phase center taken at the center element.

⁷ M. Malkomes. "Mutual Coupling Between Microstrip Patch Antennas." *Electron. Lett.*, Vol. 18 (June 1982), pp. 520-521.

⁸ S. M. Ali, T. M. Habashy, and J. A. Kong. "Resonance in Two Coupled Circular Microstrip Disk Resonators," *J. Appl. Phys.*, Vol. 53 (Sept 1982), pp. 6418-6429.

⁹ C. M. Krowne. "E-Plane Coupling Between Two Rectangular Microstrip Antennas," *Electron. Lett.*, Vol. 16 (Mar 1980), pp. 211-213.

¹⁰ C. M. Krowne and A. R. Sindoris. "H-Plane Coupling Between Rectangular Microstrip Antennas," *Electron. Lett.*, Vol. 16 (Mar 1980), pp. 211-213.

¹¹ R. E. Munson. "Conformal Microstrip Antennas and Microstrip Phased Arrays," *IEEE Trans. Antennas Propag.*, Vol. AP-22 (1974), pp. 74-78.

The array pattern can then be written as

$$F(\theta) = \frac{2\sin(k_o h \cos\theta/2)}{k_o h \cos\theta} \cos(k_o l \cos\theta/2) \sum_{n=1}^N \{ [Z_A + Z_L]^{-1} \}_{np} e^{jk_o x_n \cos\theta} \quad (8)$$

By reciprocity, Equation 8 can also be viewed as proportional to the array output voltage when the array is receiving a signal polarized in the E_z direction and incident at an angle θ . The presence of the matrix inverse in Equation 8 in general makes it difficult to display the explicit dependence of F on the reactive loads. However, for two- and three-element arrays, the inverse can be computed analytically in a reasonable fashion; in Appendix B Equation 8 is written out explicitly for these two cases.

The connection between a reactively steered array and a conventional fully driven array can be made by noting that Equation 8 can be written in the standard form of a fully driven array as

$$F(\theta) = g_e(\theta) \sum_n I_n e^{jk_o x_n \cos\theta} \quad (9)$$

in which $g_e(\theta)$ is the element pattern and the feed currents I_n are

$$I_n = \{ [Z_A + Z_L]^{-1} \}_{np} \quad (10)$$

By comparison, the feed currents of the conventional array are given simply by $I_n^{\text{conv}} = A_n = |A_n| e^{j\theta n}$, where A_n is the complex weight for the n^{th} element. The most noticeable differences between the feed currents of the reactively steered array and the conventional array are the former's nonlinear relationship between current and controlled variable (the X_i 's) and the dependence of each of its currents on all of the controlled variables.

In the simulations that follow, the incident signal and interference are both assumed to be E_z components. Additionally, a noncoherent system with a square law detector is assumed, so that the array output is computed as $V = [EE^*]^{1/2}$.

IV. ADAPTIVE CONTROL SIMULATION

A. BACKGROUND

The adaptive control discussion and simulations in this report are limited to a power inversion mode of operation for the array, in which the reactive loads are adjusted to minimize the incident interference power. This mode of operation was basically the technique used in the experimental measurements to form a null.

A generalized block diagram of a reactively steered array connected for adaptive control of the loads is shown in Figure 10. For a given

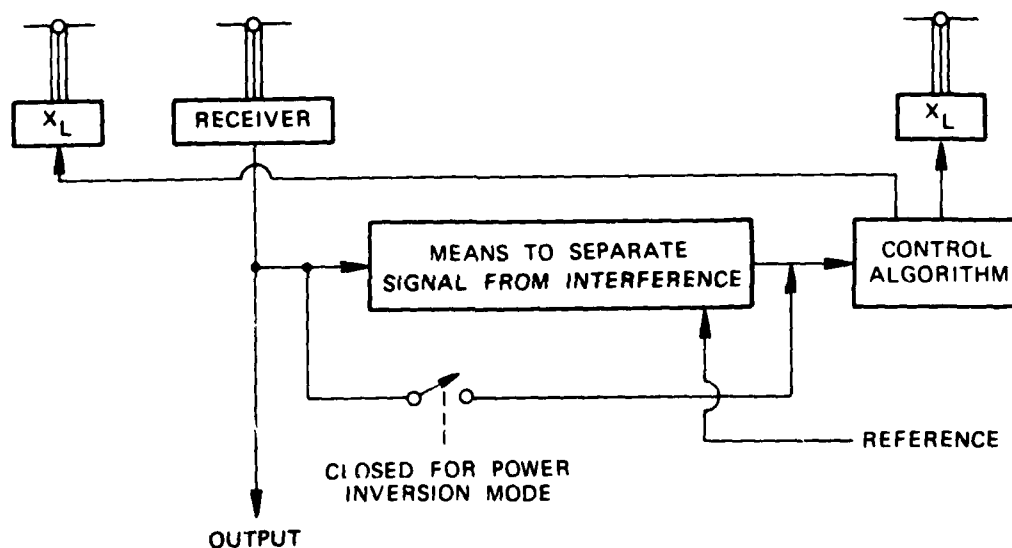


FIGURE 10. Diagram of Reactively Steered Array with a Generalized Adaptive Controller. For a mode of operation requiring a reference signal, the injection of the reference signal is indicated. However, for the measurements and analysis in this paper, no reference was used.

angle of incidence of interference, the array output as given by Equation 8 produces a surface in the N -dimensional space formed by $(N-1)$ axes for the reactive loads and one axis for the array output. This surface is the error surface for the adaptive control algorithm; the purpose of the algorithm is to find the set of reactive loads corresponding to the (hopefully single) minimum point of the error surface. Most adaptive algorithms (an exception is random search) are of the steepest descent type that find the minimum in the error surface by

beginning at some point, sensing the gradient or selected components of the gradient at that point, and incrementing the point in a direction corresponding to the steepest value of the gradient. The Widrow least mean squares (LMS) algorithm¹² in a full driven array senses the error surface gradient by correlating the outputs of each array element with the total array output and then forming an error signal. However, for the reactively steered array only the output of the single center element of the array is available, so that LMS processing is not possible.

As indicated in Figure 10, some type of modulation of the reactive loads must be provided in order to measure the gradient of the error surface. This dither signal must be applied and the resulting influence on the RESAA output measured at the same time that the interference and desired signals are being detected.

B. ERROR SURFACES

Figures 11 through 13 present examples of the error surface for a microstrip RESAA. In these figures Equation 8 is plotted for an array with the following characteristics.

- A three-element array is assumed in which each element is identical to the elements in the experimental array shown in Figure 1.
- The element spacing is the same as the experimental array in Figure 2.
- The values of $[Z_A]$ in Equation 8 are the values measured for the three center elements of the experimental array, as given in Appendix A.

For each error surface plot the angle of incidence of the signal is fixed, and Equation 8 is plotted as a function of X_1/Z_0 and X_3/Z_0 . Three different values of θ are used in the three plots.

The error surfaces for this three-element example show one well-defined global minimum that corresponds to those values of the reactive terminations that reduce the incident interference to its lowest value at the array output. The location of the minimum changes as the incidence angle changes. In Figure 14 the trace of the minimum point on the $X_1 - X_3$ plane is shown.

¹² J. E. Hudson. *Adaptive Array Principles*. London, Institution of Electrical Engineers, 1981.

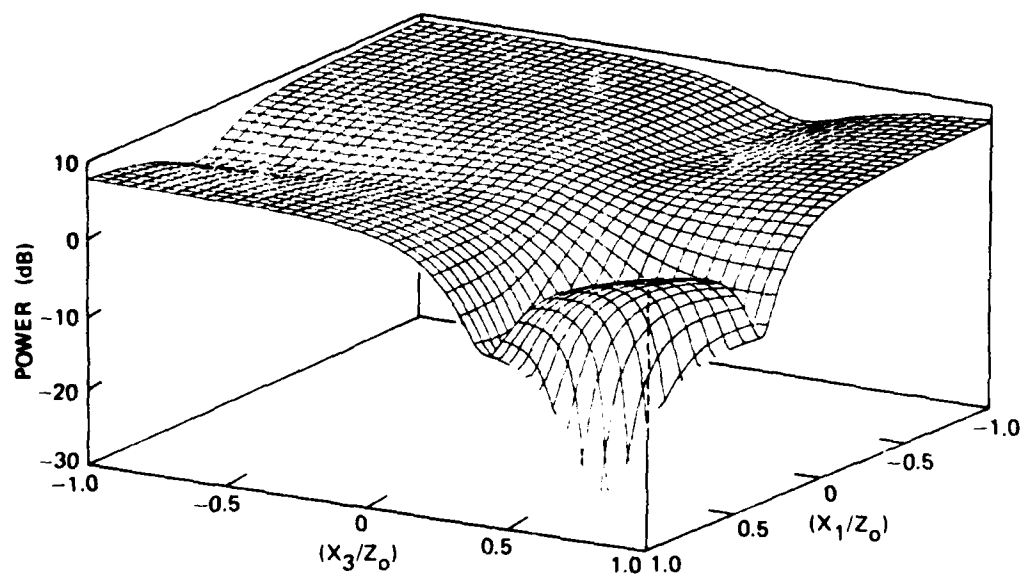


FIGURE 11. Error Surface (Array Output Versus Reactive Load Value) for a Three-Element RESAA with Interference Incident at $\theta = 0$ Degrees. 0 dB corresponds to $(E_z)_n = 1.0$ in Equation 7.

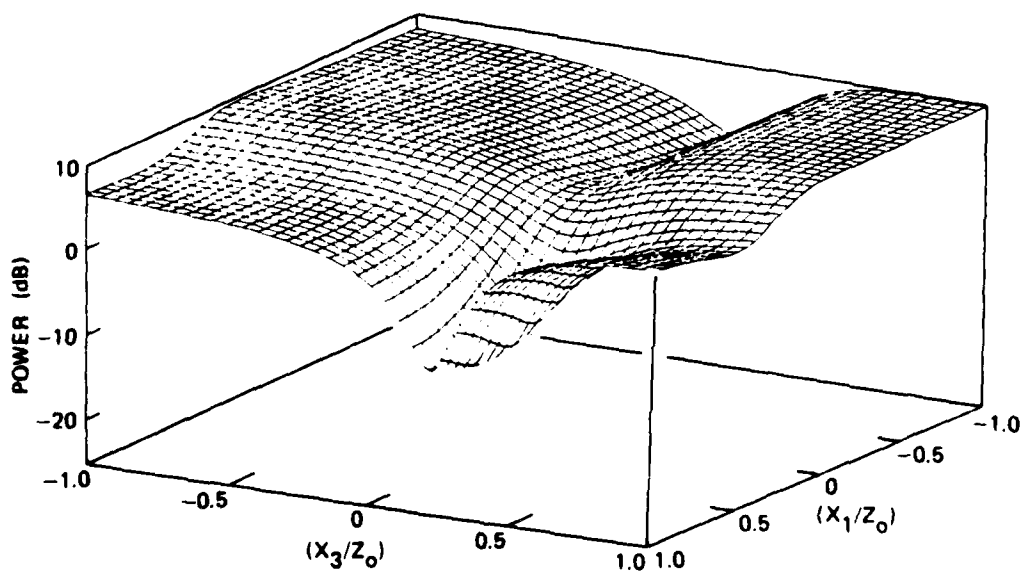


FIGURE 12. Error Surface for a Three-Element RESAA with Interference Incident at $\theta = -45$ Degrees.

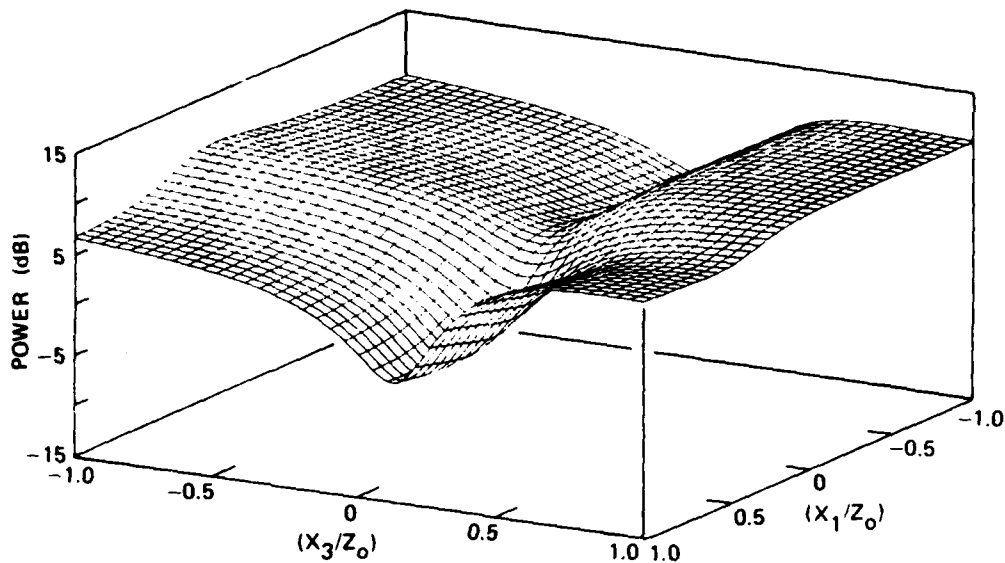


FIGURE 13. Error Surface for a Three-Element RESAA with Interference Incident at $\theta = -90$ Degrees.

C. STEEPEST DESCENT CONTROL ALGORITHM

Let $X_i(j)$ denote the reactive load on the i^{th} antenna at the j^{th} iteration. Then the discrete steepest descent algorithm states that the reactive load at the next iteration, $X_i(j+1)$, is given by

$$X_i(j+1) = X(j) - K \nabla_X \epsilon, \quad (11)$$

where K is a constant that controls the convergence rate and ϵ is the n -dimensional error surface. In terms of the error surfaces given in Figures 11 through 13, the reactive loads are adjusted to follow a path that traces out the maximum value of the gradient at every point and that proceeds to successively lower values of the array output.

In a practical implementation of steepest descent control, the partial derivative in Equation 11 can be measured by superimposing a modulation signal ΔX on the reactive load control voltage and detecting the corresponding change ΔR in receiver output; the partial derivative is approximated by $\Delta R / \Delta X$. Since the partial derivative is needed for each parasitic element, some technique must be provided to separate the responses at the receiver output for each element. Two possible methods for this separation are shown in Figures 15 and 16. For the method in Figure 15 the modulation frequency for each parasitic element is different, and synchronous detection is used to separate the response for each

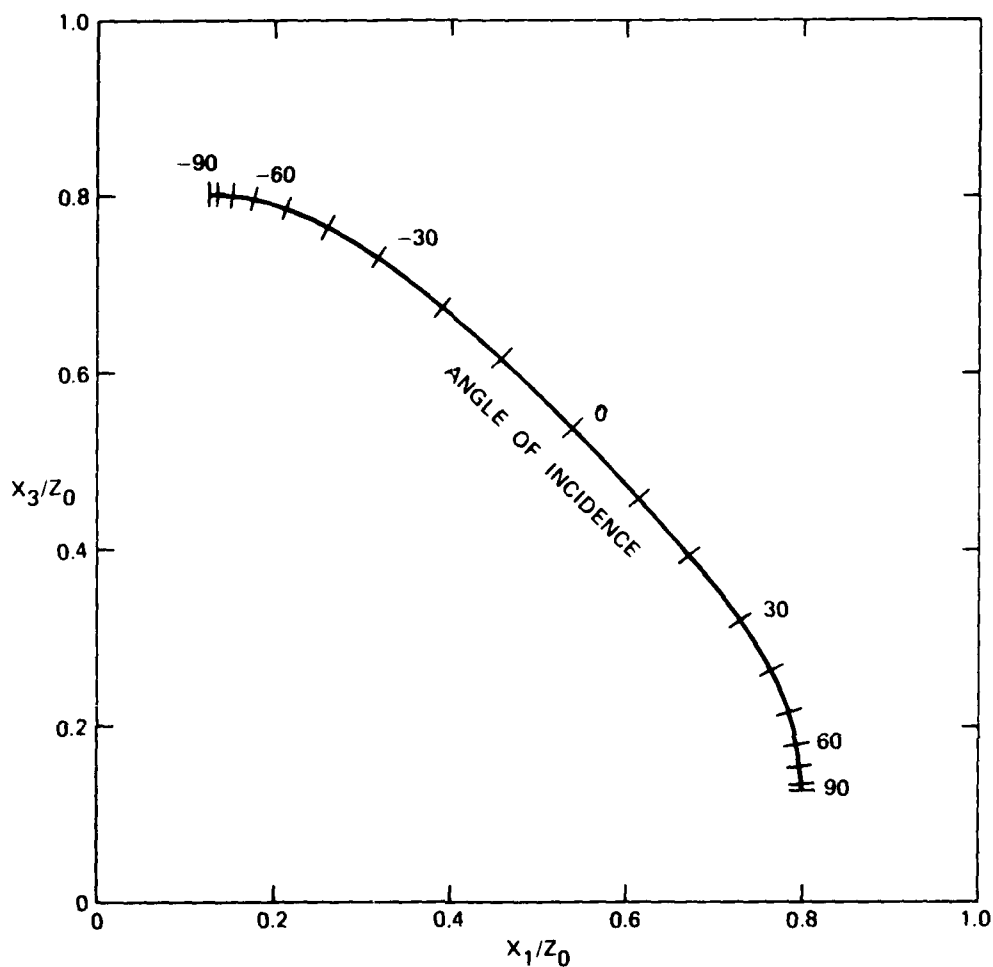


FIGURE 14. Trace of the Minimum Points in Figures 11 Through 13 on a Plane Perpendicular to the Array Output Axis.

element; this technique is probably best implemented using analog circuitry. For the method in Figure 16, the reactive loads are modulated sequentially in time, a technique that is probably best implemented using digital circuitry. The simulations discussed in the next section apply more directly to this latter technique.

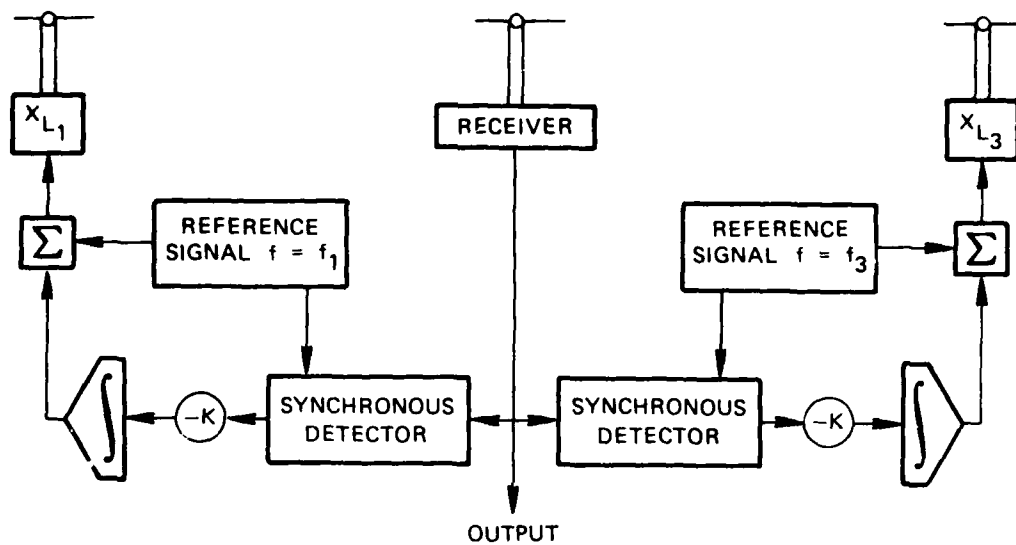


FIGURE 15. Technique for Estimating the Error Surface Slope Using a Synchronous Detector for Each Element.

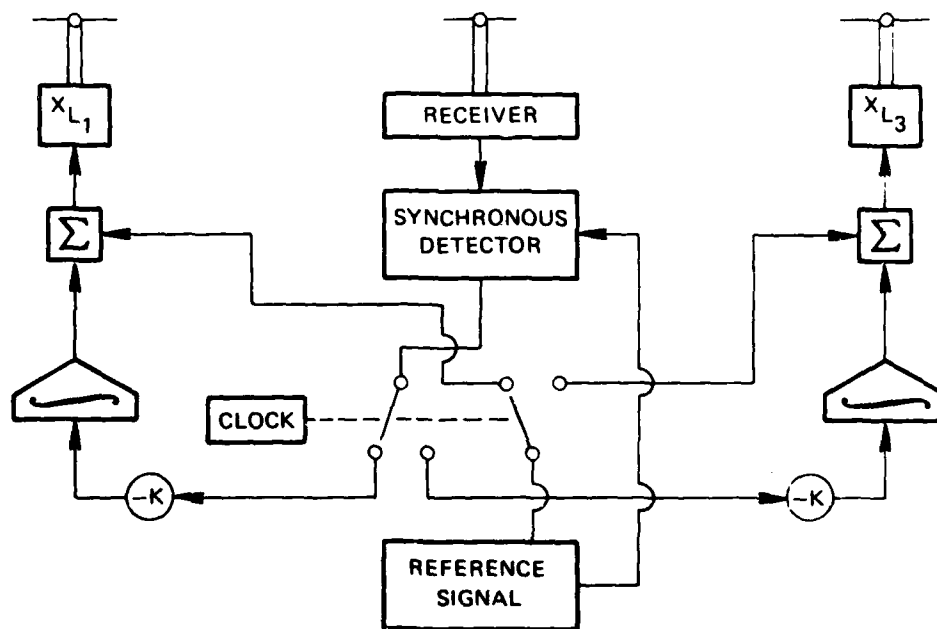


FIGURE 16. Technique for Estimating the Error Surface Slope Using One Synchronous Detector with Time Sharing Between the Elements.

D. SIMULATION RESULTS

The steepest descent algorithm was simulated on a Hewlett-Packard Model 1000 computer assuming the three-element RESAA discussed in Section IV-B. To generate the estimate of the error surface slope for Equation 11, the change in the array output in response to a small change in each reactive termination was determined at each iteration. The small change in the reactive termination is referred to as the step size, below.

Figures 17 through 19 plot the evolution of the reactive loads X_1 and X_3 during the steepest descent algorithm for three different interference angles of incidence. In all three figures the initial values

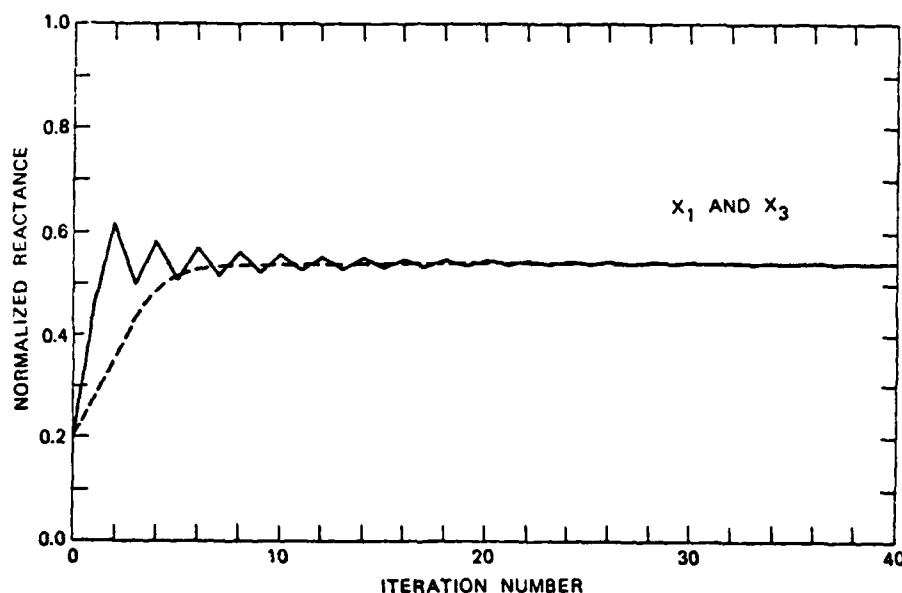


FIGURE 17. Variation of Reactive Loads During Steepest Descent Convergence on the Error Surface of Figure 11. Interference incidence angle = 0 degrees, step size = 0.01. For the dashed curve, $K = 0.01$; for the solid curve, $K = 0.035$.

of the normalized reactive loads are taken as 0.2, and curves are shown for two different values of the convergence constant K . In Figure 20 the reduction in the interference power during convergence to the error surface minimum is shown for some of the cases presented in Figures 17 through 19. Figure 21 is a display of convergence time (defined as the number of iterations needed to reach 90 percent of the final value of the reactive load) and the peak-to-peak oscillation amplitude of the steady-state reactive load value plotted as a function of the value of

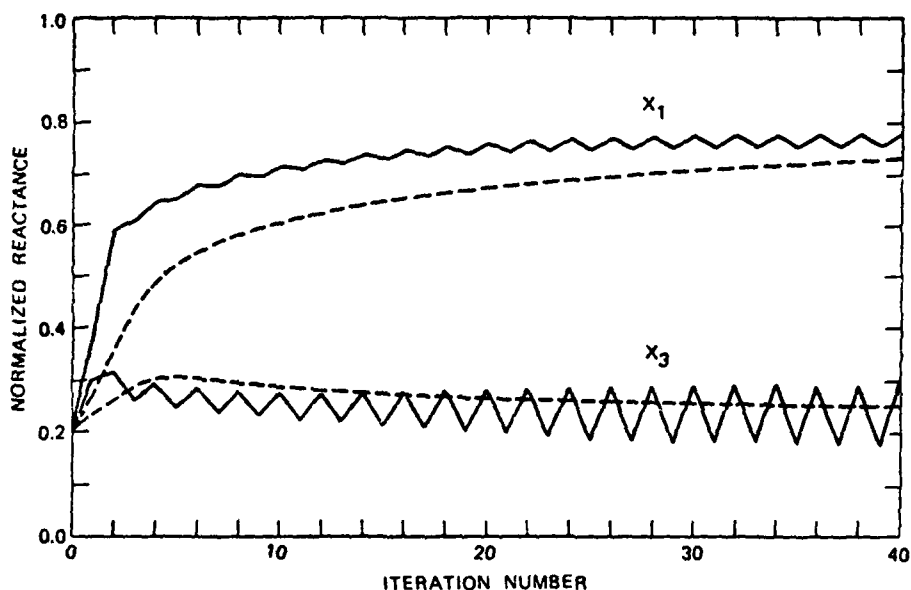


FIGURE 18. Variation of Reactive Loads During Steepest Descent Convergence on the Error Surface of Figure 12. Interference incidence angle = -45 degrees, step size = 0.01. For the dashed curves, $K = 0.01$; for the solid curves, $K = 0.028$.

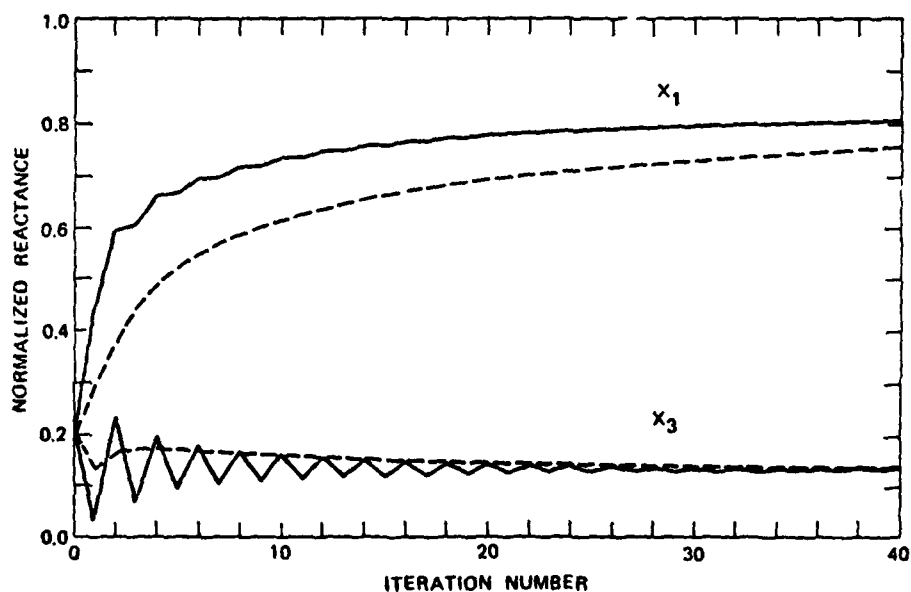


FIGURE 19. Variation of Reactive Loads During Steepest Descent Convergence on the Error Surface of Figure 13. Interference incidence angle = -90 degrees, step size = 0.01. For the dashed curves, $K = 0.01$; for the solid curves, $K = 0.025$.

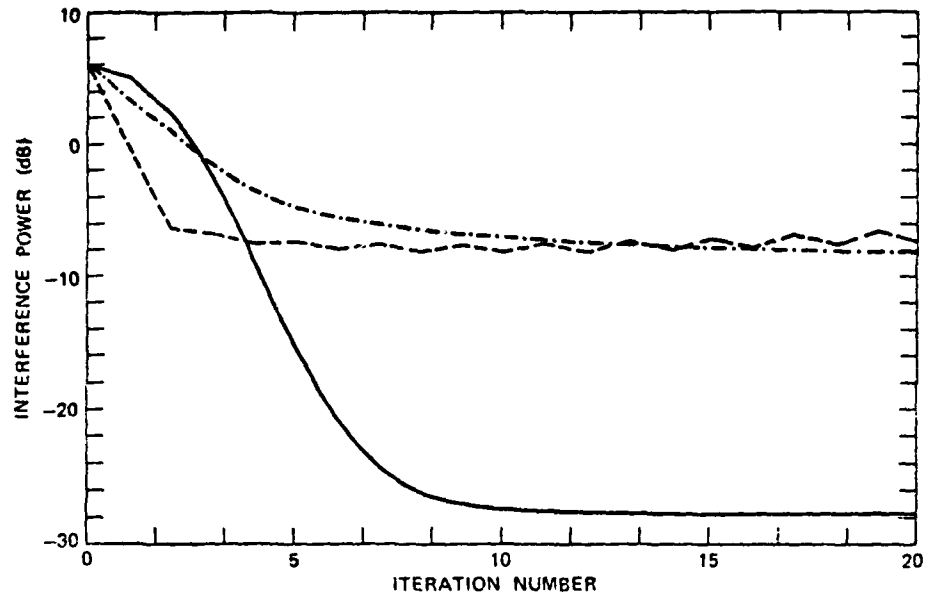


FIGURE 20. Change in Received Interference Signal Power During Steepest Descent Processing. Solid curve: interference incidence angle = 0 degrees, $K = 0.01$. Dashed curve: interference incidence angle = -45 degrees, $K = 0.028$. Dot-dashed curve: interference incidence angle = -45 degrees, $K = 0.01$.

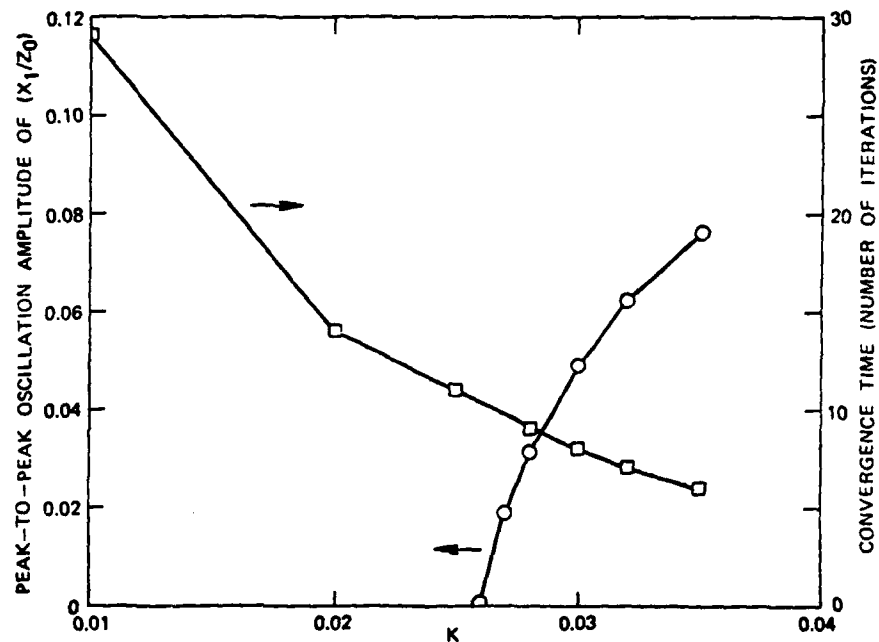


FIGURE 21. Convergence Time and Steady-State Reactive Load Jitter as a Function of K . Interference incidence angle = 0 degrees.

K. In Figures 22 through 24 we show the beam history for several selected sets of parameters. Table 1 summarizes the parameters used for Figures 17 through 24.

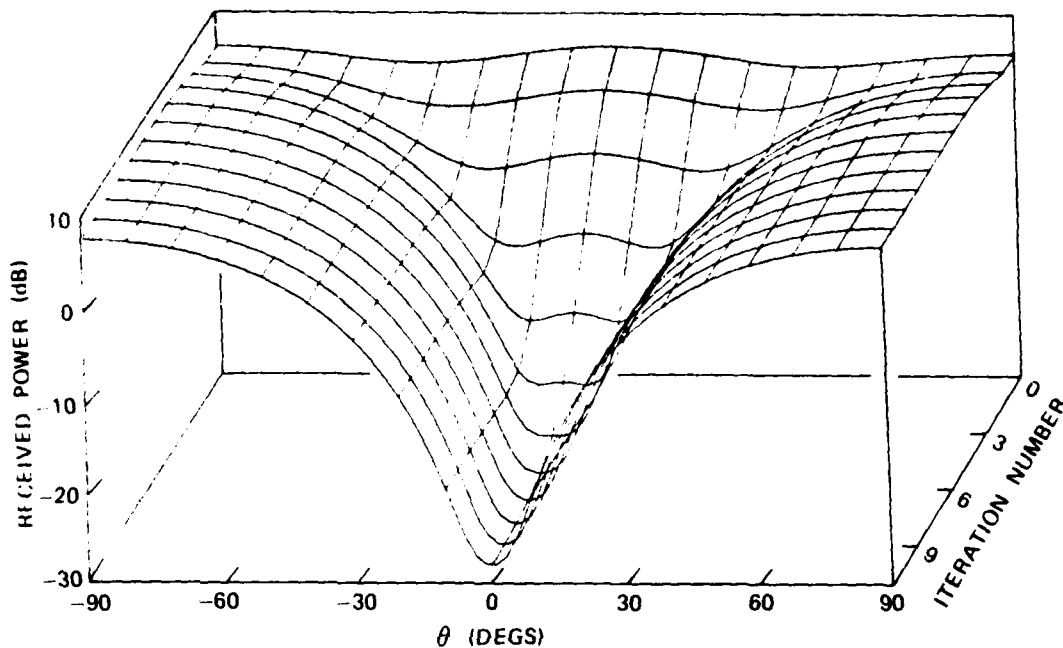


FIGURE 22. Beam History During Steepest Descent Processing for Interference Incident at 0 Degrees.

The following conclusions can be drawn from these results.

- The interference power reduction is greatest at broadside incidence (30 dB) and is least at end-fire incidence. The convergence time is related to the sharpness of the minimum (i.e., the second derivatives near the minimum); the sharper the minimum, the larger are the values of the gradient in Equation 11 for fixed K. Figures 11 through 13 show that the minimum is sharpest at broadside, which is consistent with the fast convergence.
- A trade-off between convergence speed and steady-state fluctuations in the reactive load values can be made. This kind of trade-off is usually required in adaptive antennas, and the reactively steered array is no exception.

Finally, in Figure 25 we show a beam history during steepest descent processing when two interference sources are present, one at 0 degrees and the other at -45 degrees. A three-element array does not

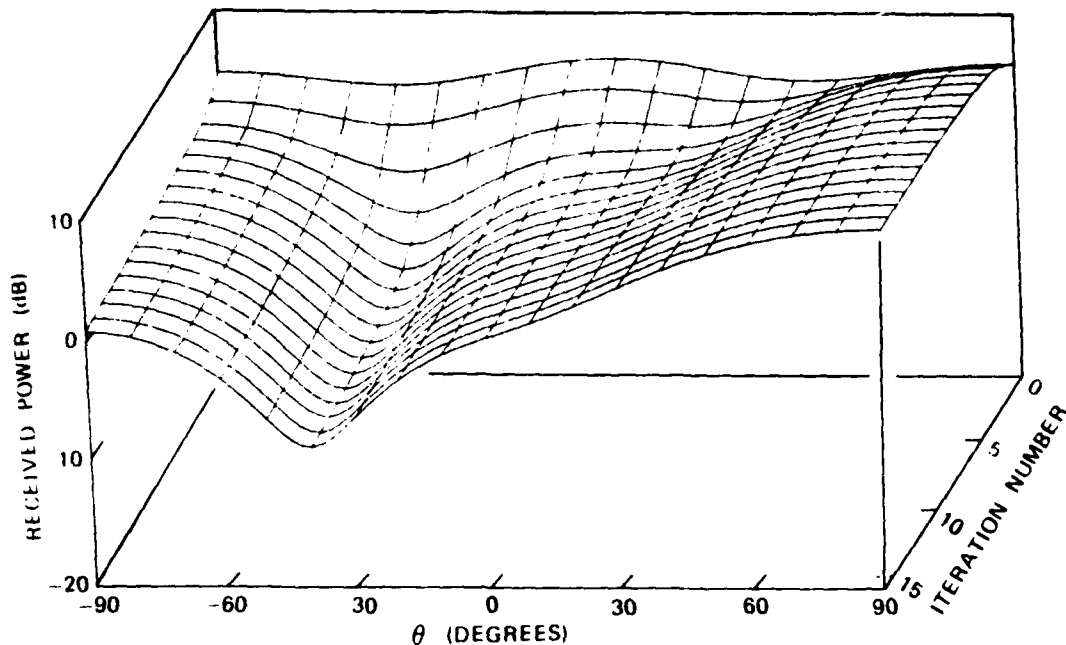


FIGURE 23. Beam History During Steepest Descent Processing for Interference Incident at -45 Degrees.

possess a sufficient number of degrees of freedom to place deep minima in the direction of both interference sources; therefore, the steepest descent algorithm does the best it can to minimize the total power.

V. CONCLUSIONS AND FUTURE PLANS

The results reported here demonstrate that a useful degree of pattern control of a microstrip adaptive array can be achieved by adjustment of the reactive loads on parasitic elements. The specific microstrip array investigated in this work could find application to missile command data links or line-of-sight communications.

The main advantage of a reactively steered adaptive array (RESAA), as compared with a conventional adaptive array, is the elimination of the mixers and other hardware needed to perform the complex weighting of the output of each element at an intermediate frequency (IF). In addition, by operating without the need for an IF and an electronic summing element, the RESAA can probably produce a larger linear dynamic range than a conventional adaptive array. We believe that a RESAA configuration can be made with substantially fewer components than a

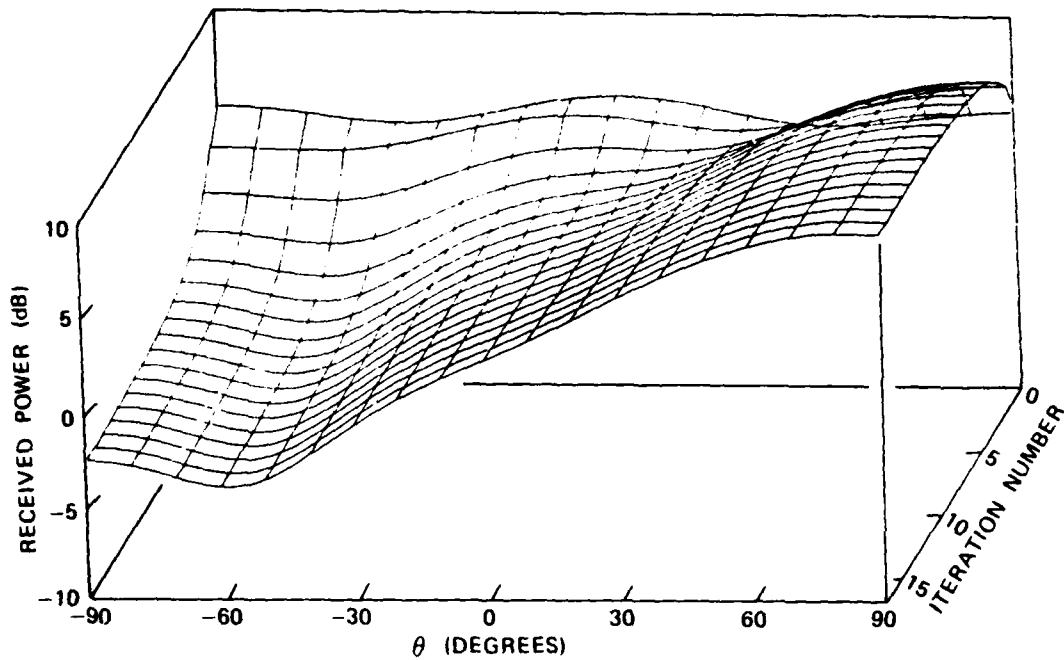


FIGURE 24. Beam History During Steepest Descent Processing for Interference Incident at -90 Degrees. For this history, only the first 17 iterations of the 50 needed to obtain a minimum at -90 degrees are shown.

TABLE 1. Summary of Parameters Used in Computations for Figures 17 Through 25.

Figure number	Interference angle of incidence, deg.	K
17	0	0.01, 0.035
18	-45	0.01, 0.028
19	-90	0.01, 0.025
20	0, -45	0.01, 0.28
21	0	variable
22	0	0.01
23	-45	0.01
24	-90	0.01
25	0, -45	0.01

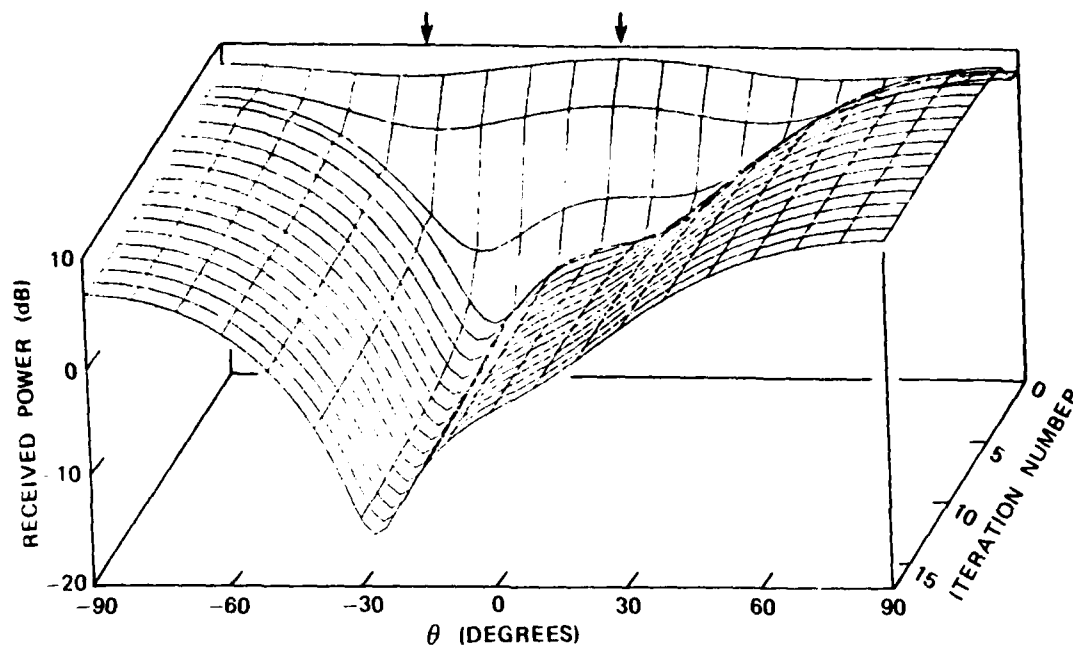


FIGURE 25. Beam History During Steepest Descent Processing for Two Equal Amplitude Interference Signals Incident at 0 Degrees and -45 Degrees.

comparable conventional adaptive array. Another advantage is the necessarily smaller overall size (needed to maintain tight coupling between elements).

There are two disadvantages to the RESAA technique: (1) Less control of the pattern is obtainable for the same number of elements, since only one control device is used for each element with the RESAA compared to the two control devices (for full complex weighting) for each element of a conventional adaptive array and (2) increased control over the pattern cannot be achieved simply by adding more elements, since new elements added at the periphery of the array have progressively less influence on the pattern.

A large number of topics relating to pattern control of a RESAA remain to be investigated and these studies are planned for FY-83. These topics include simulations with arrays of more than three elements, nulling of more than one interference source, the effect of Gaussian noise on performance, bandwidth achievable with RESAAs, the equivalent number of degrees of freedom that can be realized, and the practical aspects of implementing an experimental RESAA with automatic control.

Appendix A

MEASUREMENT OF MUTUAL IMPEDANCE MATRIX ELEMENTS USING
AN AUTOMATIC NETWORK ANALYZER

The mutual impedance matrix elements required for Equation 2, Z_{mn} , are difficult to calculate for microstrip patch antenna elements. For the simulations reported here, measurements were made on the array shown in Figure 1, and these values were used in the simulation.

A Hewlett-Packard (HP) Model 8410 network analyzer controlled by an HP-9825 calculator was used to measure the scattering parameters of the array. Measurements of S11 at each port were made with all other element feed ports terminated in 50-ohm loads. Measurements of S21 were made pairwise between ports, with the remaining ports terminated in 50-ohm loads. These measurements of S11 and S21 then are entries in the scattering matrix [S].

To obtain the elements of the impedance matrix [Z], the following equation is used:¹³

$$[Z] = [I + S][I - S]^{-1}, \quad (A-1)$$

where [I] is the identity matrix. Table A-1 lists the values of the elements of [Z] obtained in this manner for the three center elements. These values were used in the simulations.

TABLE A-1. Measured Values of the Mutual Impedance Matrix [Z] Normalized to a Resistance of 1 ohm.

Matrix element	Real part	Imaginary part
Z(11),Z(33)	0.273	-0.227
Z(22)	0.240	-0.260
Z(12),Z(21),Z(23),Z(32)	0.138	0.108
Z(13),Z(31)	0.00780	-0.0982

¹³ R. E. Collin. *Field Theory of Guided Waves*. New York, McGraw-Hill, 1960.

Appendix B

RADIATION PATTERNS FOR TWO- AND THREE-ELEMENT REACTIVELY STEERED ADAPTIVE ARRAYS

The matrix inverse that appears in Equation 8 in general cannot be simplified in any manner that shows more clearly the dependence of the radiation pattern on the reactive loads. However, for two- and three-element arrays, the matrix inverse can be computed explicitly. This Appendix gives the radiation patterns for these cases.

TWO-ELEMENT ARRAY

For a two-element array, the inverse is required of the matrix:

$$[Z_A + Z_L] = \begin{bmatrix} Z_{11} & Z_{12} \\ Z_{12} & Z_{11} + Z_L \end{bmatrix}, \quad (B-1)$$

where element-1 is assumed to be driven and element-2 has a reactive load Z_L . The inverse matrix is given by

$$[Z_A + Z_L]^{-1} = \frac{1}{D} \begin{bmatrix} Z_{11} + Z_L & -Z_{12} \\ -Z_{12} & Z_{11} \end{bmatrix}, \quad (B-2)$$

in which $D = \det(Z_A) + Z_{11}Z_L$. For an element separation of d , the pattern can be written out in full as

$$F(\theta) = \frac{g_a(\theta)}{D} \left[Z_{11} + Z_L - Z_{12} e^{jk_o d \sin \theta} \right], \quad (B-3)$$

where $g_a(\theta)$ is the element pattern.

THREE-ELEMENT ARRAY

The inverse is required of the matrix given by

$$[Z_A + Z_L] = \begin{bmatrix} Z_e + L_1 & Z_1 & Z_2 \\ Z_1 & Z_m & Z_1 \\ Z_2 & Z_1 & Z_e + L_3 \end{bmatrix}, \quad (B-4)$$

where Z_e is the self-impedance of the end elements, Z_m is the self-impedance of the middle element, Z_1 is the mutual impedance between nearest neighbors, Z_2 is the mutual impedance between the end elements, and L_1 and L_3 are the reactive loads on element-1 and -3, respectively. The inverse is given by

$$[Z_A + Z_L]^{-1} = \frac{1}{D} \begin{bmatrix} Z_m(Z_e + L_3) - Z_1^2 & Z_1 Z_2 - Z_1 Z_e - Z_1 L_3 & Z_1^2 - Z_2 Z_m \\ Z_1 Z_2 - Z_1 Z_e - Z_1 L_3 & Z_e^2 + Z_e L_3 + Z_e L_1 + L_1 L_3 - Z_2^2 & Z_1 Z_2 - Z_1 Z_e \\ Z_1^2 - Z_2 Z_m & Z_1 Z_2 - Z_1 Z_e - Z_1 L_1 & Z_e Z_m + L_1 Z_m - Z_1^2 \end{bmatrix} \quad (B-5)$$

in which D is the determinant of the matrix $[Z_A + Z_L]$. The pattern then can be written as

$$F(\theta) = \frac{g_a(\theta)}{D} \left\{ [Z_m(Z_e + L_3) - Z_1^2] e^{-jk_o d \sin \theta} + Z_1(Z_2 - Z_e - L_3) + [Z_1^2 - Z_2 Z_m] e^{jk_o d \sin \theta} \right\}. \quad (B-6)$$

INITIAL DISTRIBUTION

- 8 Naval Air Systems Command
 - AIR-00D4 (2)
 - AIR-03C, G. Heiche (1)
 - AIR-03P2X, R. Thyberg (1)
 - AIR-33A, F. J. Lueking (1)
 - AIR-33R, J. Willis (1)
 - AIR 332C, A. Glista (1)
 - AIR-360F, C. Caposell (1)
- 5 Chief of Naval Operations
 - OP-0941 (1)
 - OP-0944 (1)
 - OP-098 (1)
 - OP-0986 (1)
 - OP 987 (1)
- 7 Chief of Naval Research, Arlington
 - ONR-200, J. O. Dimmock (1)
 - ONR-210B, LCDR T. L. Swafford (1)
 - ONR-250, CDR D. S. Siegal (1)
 - ONR-414
 - L. Griffiths (1)
 - D. Lewis (1)
 - J. Wright (1)
 - ONR-430, A. M. Diness (1)
- 4 Naval Electronics System Command
 - Code 61A (1)
 - Code 611, B. Hughes (1)
 - Code 614, J. Cauffman (1)
 - Code PME-109-20, R. Eisenberg (1)
- 4 Naval Sea Systems Command
 - SEA-62R1
 - C. E. Jedrey (1)
 - T. Tasaka (1)
 - SEA-99612 (2)
- 1 Commander in Chief, U. S. Pacific Fleet (Code 325)
- 1 Commander, Third Fleet, Pearl Harbor
- 1 Commander, Seventh Fleet, San Francisco
- 3 Naval Air Development Center, Warminster
 - A. T. Cerino (1)
 - H. H. Heffner (1)
 - G. T. Piffung (1)
- 1 Naval Ocean Systems Center, San Diego, (P. Hansen)
- 7 Naval Research Laboratory
 - Code 7500, J. R. Davis (1)
 - Code 7550
 - D. Himes (1)
 - W. Meyers (1)
 - L. Wagner (1)
 - W. Gabriel (1)
 - F. F. Kretschmer (1)
 - C. M. Krowne (1)

3 Naval Ship Weapon Systems Engineering Station, Port Hueneme
 Code 5711, Repository (2)
 Code 5712 (1)
 1 Naval War College, Newport
 1 Office of Naval Technology, Arlington (MAT-073)
 1 Pacific Missile Test Center, Pt. Mugu (C. Kalot)
 1 Army Research Office, Research Triangle Park (J. W. Mink)
 1 Harry Diamond Laboratories, Adelphi (A. R. Sindoris)
 2 Rome Air Development Center, Griffis Air Force Base
 DCCR, J. A. Granero (1)
 OCTS, V. Vannicola (1)
 1 Rome Air Development Center, Hanscom Air Force Base (R. Mailloux)
 12 Defense Technical Information Center
 1 General Atomics Corporation, Philadelphia, PA (L. R. Burgess)
 2 Lincoln Laboratory, MIT, Lexington, MA
 J. T. Mayhan (1)
 A. Simmons (1)
 1 New Mexico State University, Physical Science Laboratory, Las Cruces, NM (K. R. Carver)
 1 Ohio State University, ElectroScience Laboratory, Columbus, OH (R. T. Compton)
 1 Stanford University, Department of Electrical Engineering, Stanford, CA (B. Widrow)
 1 Syracuse University, Department of Electrical and Computer Engineering, Syracuse, NY (R. A. Harrington)
 2 University of California, Electrical Sciences and Engineering Department, Los Angeles, CA
 N. G. Alexopoulos (1)
 R. S. Elliott (1)
 1 University of Colorado, Electromagnetics Laboratory, Boulder, CO (D. C. Chang)
 1 University of Houston, Department of Electrical Engineering, Houston, TX (S. A. Long)
 1 University of Pennsylvania, Moore School of Electrical Engineering, Philadelphia, PA (B. D. Steinberg)
 1 Zeger-Abrams Inc., Glenside, PA (A. E. Zeger)

